Chapter

Metasurfaces for Structured Terahertz Waves: Generation, Control and Applications

Wei Chen, Zhong-Ze Peng, Ling-Ling Ma and Yan-Qing Lu

Abstract

Terahertz (THz) structured fields, such as vortex beams carrying orbital angular momentum, Bessel beams, and vector beams, support mode multiplexing, extended depth of focus, and improved scattering tolerance in communication, sensing, and imaging. Metasurfaces, consisting of ultrathin subwavelength arrays, employ metallic or all-dielectric building blocks to enable wavefront manipulation through geometric-phase or resonance mechanisms. Building on these foundations, subsequent research has sought to further enhance functionality and efficiency by developing multilayer configurations that integrate multiple operations and support more complex modulation. In parallel, tunable materials – such as phase-change compounds, liquid crystals, and graphene, whose properties respond to external physical stimuli – have been incorporated to dynamically control optical responses. These approaches enable planar, programmable manipulation of phase, amplitude, and polarization in the THz regime while reducing losses and device footprint, thereby providing reconfigurability beyond that of conventional bulk optics. The chapter summarizes recent advances in THz metasurfaces for structured beams along four themes: high-efficiency beam-shaping mechanisms; control strategies using tunable materials and reconfigurable architectures; multifunctional integration incorporating frequency, polarization, and mode multiplexing; and applications in communication, imaging, and high-field emission. We discuss the future directions for scalable, tunable, and efficient platforms to facilitate chip-to-free-space interfaces, metrology, and manufacturable implementation. Two noteworthy areas of interest are ferroelectric nematic liquid-crystal platforms and spatiotemporally structured THz waves, which are also discussed.

Keywords: terahertz metasurfaces, structured beams, orbital angular momentum, tunable and programmable control, multifunction integration

1. Introduction

Terahertz (THz) radiation (0.1–10 THz) occupies the spectral gap between microwaves and the infrared. It combines an underexploited bandwidth, low photon energy, and strong penetration through most nonmetallic materials and is widely viewed as a bridge between electronic and photonic technologies [1–3]. At the application level, THz waves address spectral fingerprints of molecular rotations and lattice vibrations, enabling chemically selective biosensing and nondestructive quality inspection [4–8]. At the information level, tens to hundreds of gigahertz of contiguous bandwidth provide the physical basis for Tb/s-class wireless links and short-reach backhaul in 6 G/6 G + [9, 10]. At the physics level, single-cycle or broadband THz pulses drive strong-field nonlinearities and ultrafast dynamics of electronic, lattice, and spin degrees of freedom, opening a key window between classical electromagnetism and quantum material responses [11]. However, conventional Gaussian beams limit capacity, robustness, and wave–matter interaction strength: limited spatial modes and polarization degrees of freedom, together with sensitivity to scattering and turbulence, hamper stable high-dimensional transport in complex links and heterogeneous samples.

Structured THz fields offer three complementary degrees of freedom. First, vortex beams carrying orbital angular momentum (OAM) form a near-orthogonal eigenmode set under suitable aperture and alignment; modes with distinct topological charge l can be multiplexed at a single frequency and polarization to extend channel count in spectrum-limited links [12, 13]. Second, nondiffracting and self-accelerating beams, such as Bessel and Airy, provide extended depth of field (DOF) and reduced sensitivity to partial occlusion and diffraction, aiding imaging and detection on curved or scattering surfaces [14–16]. Third, vector-polarized fields – radial, azimuthal, and generalized Poincaré states – enable tailored transverse and longitudinal components, improving coupling for chiral recognition, anisotropic material characterization, and micro/nano manipulation [17, 18]. These features address, respectively, mode capacity, propagation robustness, and field–matter coupling, and can be combined in system design as permitted by mode purity, alignment tolerance, scattering strength, and device bandwidth.

Realizing this potential at THz frequencies requires addressing gaps in material response. Natural media offer limited tunable dispersion at sub-millimeter wavelengths; bulk optics are large, lossy, and constrained in phase continuity and dispersion control; and tunable devices (phase shifters, spatial light modulators) remain immature in the THz range, making it difficult to co-optimize refresh rate, phase accuracy, and aperture. Atmospheric absorption and multipath scattering further degrade links, complicating the simultaneous pursuit of high efficiency, broad bandwidth, and programmability. Progress must proceed in concert across materials, structures, and systems: low-loss and tunable materials; subwavelength phase and mode engineering; and programmable, algorithm-assisted optimization at the system level.

Metasurfaces built from subwavelength meta-atoms have therefore emerged as a key platform for THz wavefront engineering [19, 20]. By co-designing Pancharatnam–Berry (PB) geometric phase, resonance-based phase, and higher-order multipolar interference, metasurfaces can simultaneously manipulate amplitude, phase, polarization, and OAM within subwavelength thickness, enabling planar, full-parameter control across free-space and surface waves, scalar and vector fields, and single-mode and multiplexed operation [21, 22]. Compared with bulk components, metasurfaces offer three system-level advantages: (i) ultrathin yet high-phase-coverage – achieving 2π and even multi-turn phase coverage with electromagnetic thickness far below the wavelength; (ii) compatibility with multiple actuation mechanisms – readily integrated with phase-change media, two-dimensional materials, liquid crystals (LCs), and semiconductors for thermal, electrical, optical, and magnetic actuation; and (iii) programmable and manufacturable – supporting rapid wavefront customization via discrete/continuous geometric encoding, and scalable production and on-chip integration via 3D printing and CMOS-compatible processes [19, 20].

Building on this base, structured THz fields have moved from static to active control, with early signs of intelligent operation. Initial studies used passive geometric phase and metallic or dielectric resonators to impose fixed wavefronts, enabling efficient generation of vortices, Bessel beams, and vector fields [23–26]. Tunable media, such as graphene and liquid crystals (LCs), then introduced thermal, electrical, optical, and magnetic bias for phase reconfiguration, mode switching, and multi-channel multiplexing [27–30]. In parallel, nonlinear generation shifted wavefront design upstream to the near-infrared: optical rectification (OR) and difference-frequency generation (DFG) transfer near-infrared (NIR) phase and polarization coding to THz with high fidelity, linking emission and control [31]. More recently, topological photonics and non-Hermitian phase engineering have provided disturbance-tolerant control of chirality and phase in the THz, pointing to higher-purity modes, multimode transport, and more robust propagation [32].

In line with this logic, the chapter moves from underlying mechanisms to control approaches, then to system design, and finally to multifunctionality and applications. Section 2 addresses high-efficiency generation of structured THz waves under material and dispersion constraints. Section 3 covers on-demand control of phase, polarization, and modes using tunable materials and programmable architectures. Section 4 discusses multifunctional integration and system-level design spanning multi-channel and polarization multiplexing. Section 5 interfaces these capabilities with forefront applications in communications, imaging, and strong-field science. Section 6 outlines coordinated strategies and standardization toward the concurrent goals of high efficiency, broad bandwidth, and programmability. Our aim is to unify dispersed device-level advances into a clear mechanism–function–application map, providing actionable pathways from principle to engineering for structured THz fields using metasurfaces.

2. Generation mechanisms

Structured THz fields have progressed along two complementary tracks. The first is passive wavefront engineering, which achieves high efficiency and high mode purity without time-varying drives by using static metasurfaces or photonic crystals. The second is active and programmable generation, which introduces the time dimension and cross-band mapping into the "generation–shaping" pipeline via nonlinear frequency conversion or tunable materials. These routes are not oppositional; rather, they are cascaded or hybridized under different task constraints and system trade-offs, jointly serving communications, imaging, and strong-field control.

2.1 Passive wavefront engineering

The passive approach relies on PB geometric phase and resonance phase to deliver reproducible wavefronts in fixed devices. Li et al. theoretically analyzed and numerically simulated a metasurface–dielectric–metal reflective PB metasurface with orthogonal I-shaped elements, converting circular polarization into multi-order OAM across 0.8–1.4 THz with simulated reflectance >90% and an approximately linear PB phase response (**Figure 1a**) [33]. Extending this idea, Guo et al. theoretically designed and numerically validated a reflective PB metasurface producing $l = 1$ and $l = 2$ vortices over 0.9–1.8 THz, with simulated efficiencies exceeding 90% [25]. In transmission, Niu et al. experimentally realized broadband THz vortex generation (0.5–1 THz) using a three-layer Fabry–Perot cavity comprising orthogonal gratings and split-ring resonators, achieving a peak efficiency of ~ 65% at 0.5 THz and demonstrating mechanical flexibility for conformal use (see **Figure 1b**) [23]. Fan et al. experimentally demonstrated quasi-perfect vortices at 0.75 THz using all-dielectric high-index silicon pillars, demonstrating multi-channel quasi-perfect vortices and spin-distinguished superposed polarization vortices (**Figure 1c**) [34]. Beyond geometric and resonant phase, Bai et al. theoretically employed bound states in the continuum (BIC) in photonic crystal slabs to access high-Q modes and, in simulations, generate high-purity, higher-order THz vortex radiation (**Figure 1d**) [35].

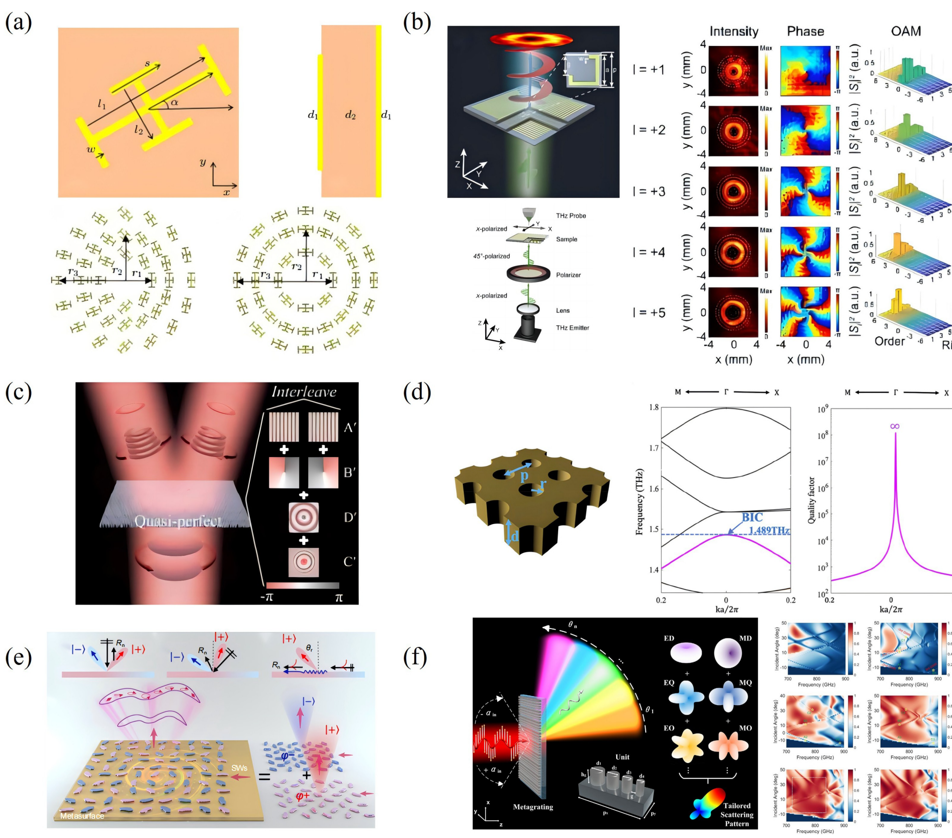

Figure 1.
Passive wavefront engineering of structured THz waves. (a) Metasurface unit and reflective PB design [33]. (b) THz vortex plates [23]. (c) Metasurface-based multi-channel quasi-perfect vortex beams [34]. (d) Photonic crystal with BIC for high-purity vortex radiation [35]. (e) SW-mediated vector-field generation [36]. (f) Asymmetric all-dielectric supergrating [37].

Balancing efficiency and directivity is important in passive devices. Wang et al. reported surface-wave (SW)-mediated, spin-selective on-chip–to–free-space launchers: experiments showed single-spin emission with ~ 90–95% relative efficiency (absorption excluded) at ~ 0.4 THz, and a dual-channel implementation driven by a common SW generated a radially polarized Bessel beam with high directivity and near-nondiffracting behavior (**Figure 1e**) [36]. Using an all-dielectric asymmetric supergrating, Peng et al. exploited octupole-assisted multipolar interference to achieve bi-asymmetric scattering and suppress parasitic channels, directing >80% efficiency into the – 1 diffraction order and realizing wide-angle, broadband steering across ~ 0.70–0.85 THz (**Figure 1f**) [37]. In general, passive platforms offer low insertion loss, wafer-scale apertures, and high mode purity, which make them well-suited as fixed front- or back-end modules and as on-chip out-/in-coupling interfaces. Their limitations include a lack of temporal reconfigurability and limited programmability, which often motivates cascading with active stages for adaptive operation and fast multimode switching.

2.2 Active and programmable generation

Active approaches provide flexibility and cross-band capability primarily through optical-domain encoding followed by nonlinear conversion. Spatial phase and/or polarization patterns are first sculpted at near-infrared or visible wavelengths and then transferred to the THz regime via DFG or OR, enabling complex THz wavefronts under broadband pulse excitation. In a DFG scheme, Yuan and Xu' group used two pumps carrying independent phase/polarization profiles and, under type-II phase matching, realized arithmetic combinations of spatial wavefronts, reproducing vortices, Bessel beams, and hybrid states in the THz with high fidelity; the topological charge is continuously tunable while maintaining quasi-nondiffracting propagation (**Figure 2a**) [31]. In an OR scheme, Dhaybi et al. used vector pumps such as radial polarization and mapped their spatial phase/polarization to the THz via $\chi^{(2)}$ rectification in [110]-cut ZnTe, generating quasi-monochromatic THz vortex beams; by rotating a polarizer and filtering in the Fourier plane, they demonstrated switching between $l = +2$ and $l = -2$, indicating effective mapping from vector pumps to THz vortex and polarization states [38]. Moreover, Mou et al. used a liquid-crystal-polymer q-plate to imprint OAM on an 800-nm pump (e.g., $l_{\mathrm{p}} = +1$) and achieved broadband (≈0.1–3 THz) $\chi^{(2)}$ rectification in a 111-cut ZnTe; measurements established $l_{\mathrm{THz}} \approx -2l_{\mathrm{p}}$, and rotating the pump polarization rotated the THz vector field, manifested as a coordinated rotation of the four-lobe transverse pattern [39].

Nonlinear metasurfaces integrate phase engineering at the emitter: McDonnell et al. employed PB phase in a C3 nano-antenna nonlinear array to emit THz vortex pulses with spin–orbit decoupling, enabling independent control over frequency, spin, and OAM (**Figure 2b**) [40]. Niu et al. programmed the local nonlinear PB phase via meta-cell orientation and combined it with pump-side DMD spatial gating to realize a 2-bit programmable THz phased array, experimentally demonstrating single/dual-beam synthesis, OAM generation, and scanning slit imaging across 0.8–1.4 THz, while avoiding RF phase-shifter insertion loss and maintaining broadband pulse characteristics (**Figure 2c**) [41]. In the high-field

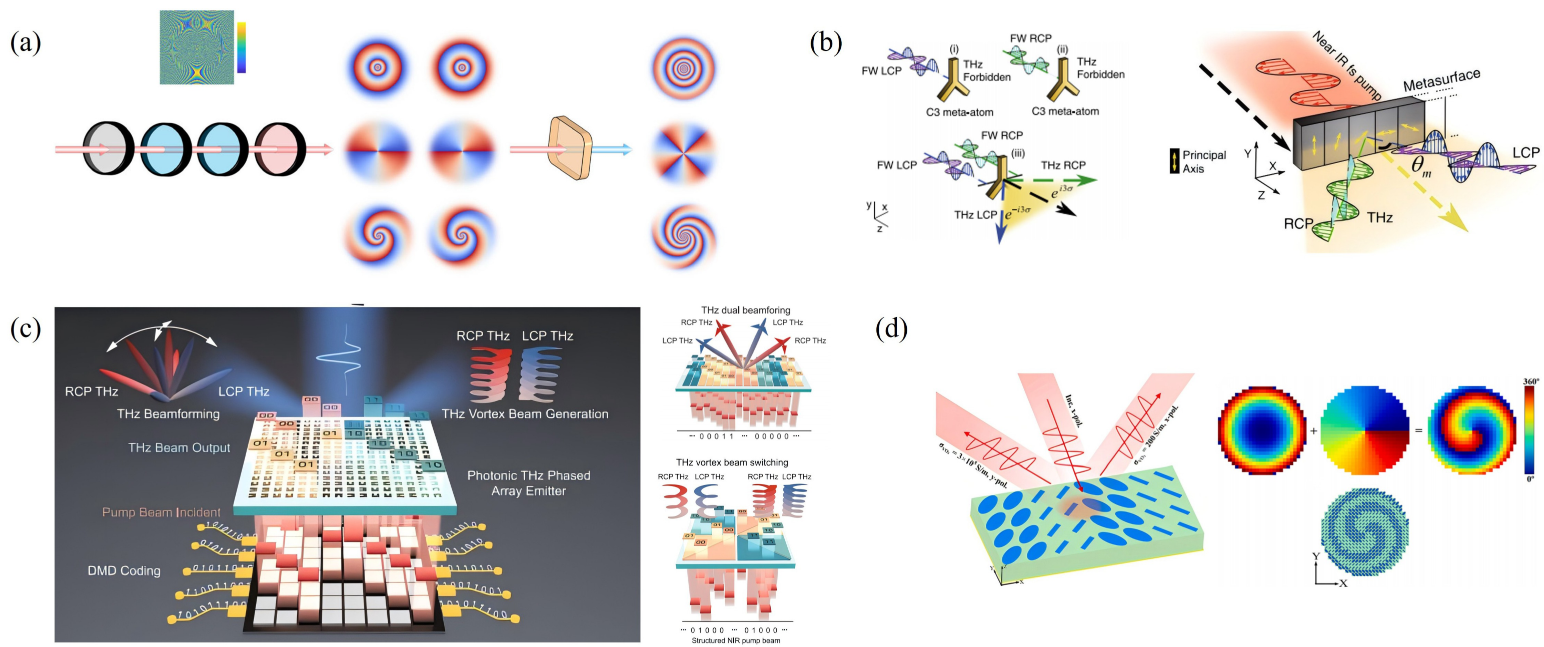

Figure 2.
Active, programmable structured THz generation via optical encoding and nonlinear conversion. (a) DFG transfer of optical phase/polarization to THz [31]. (b) Nonlinear PB-phase metasurface emitting THz vortices [40]. (c) Programmable OAM and beam profiles enabled by meta-cell orientation plus DMD-gated pumping [41]. (d) High-field plasma-channel source producing tunable fractional-OAM THz pulses [42].

regime, Wang et al. theoretically and numerically demonstrated plasma-channel–mediated THz emission in which phase matching and plasma dispersion enable high-field vortex pulses with fractional/near-integer OAM; the topological charge was tuned continuously from about − 2 to + 2 by adjusting the laser injection (offset/incident angle), providing a high-field OAM source relevant to strong-nonlinear spectroscopy and field-driven matter studies (**Figure 2d**) [42].

3. Control and reconfiguration strategies

Once structured THz fields can be generated reliably, a central question is how to reconfigure the wavefront on relevant time scales and across use cases. Progress broadly follows two directions: (i) material-centric tuning, which employs phase transitions, carrier modulation, and magneto-optic effects to add temporal control and multimodal multiplexing; and (ii) programmable architectures, which introduce real-time shaping and feedback through reconfigurable metasurfaces and phased arrays.

3.1 Tunable materials for phase, polarization, and mode control

Phase-change and carrier-tunable media offer response times ranging from milliseconds to sub-nanoseconds, with trade-offs among ON/OFF contrast, phase coverage/continuity, and energy cost. Using the VO_2 metal–insulator transition, Dong et al. realized thermally switchable PB-phase THz metasurfaces that toggle among anomalous refraction (±1 diffraction orders), vortex beams with $l = \pm 1$, and holographic reconstructions near 0.6 THz (**Figure 3a**) [43]. Guo et al. demonstrated a VO_2-based, thermally driven THz metasurface that allocates OAM across six channels with sign inversion, achieving $l = -3/-2/-1$ (metallic state) and $l = +1/+2/+3$ (insulating state) over 1.35–1.39 THz (**Figure 3b**) [44]. With electrostatic Fermi-level tuning in graphene, Ma et al. [45] and Chen et al. [27] numerically demonstrated rapid switching of THz topological charge at 2–2.4 THz and 4.5–5.5 THz, respectively, while preserving linear polarization (**Figure 3c**). Wang et al. experimentally demonstrated a cascaded dielectric–LC–plasmonic metadevice that generates near-field (plasmonic) and far-field (free-space) multi-order vortices over 0.44–0.52 THz, and electrically selects among 12 vortex modes via LC reorientation, showcasing near/far-field integration with low-voltage control (**Figure 3d**) [46]. Zhao et al. experimentally introduced tunable chirality by coupling an LC-integrated asymmetric metasurface to a helical phase layer to control spin–orbit interaction, achieving active interconversion between $l = \pm 2$ vortices and cylindrical vector beams with excitation efficiencies up to ~92% and modulation depths up to ~72% (**Figure 3e**) [47]. Extending this stack, Zhao et al. built an electrically controlled spiral-phase/LC/focusing-lens assembly that independently addresses RR/RL/LL/LR spin channels (right–right, right–left, left–left, and left–right circular polarization, denoting input–output) over 0.4–0.6 THz, with 94% peak efficiency, > 80% purity for $l = 2, -1, 0, 1$, and dynamic dual-focal switching (**Figure 3f**) [48].

For thermal platforms, Yang et al. numerically leveraged the temperature-dependent plasma frequency and loss of InSb to implement broadband vortex phase engineering, thermally tuning operation from 1.8 to 4.5 THz while maintaining high

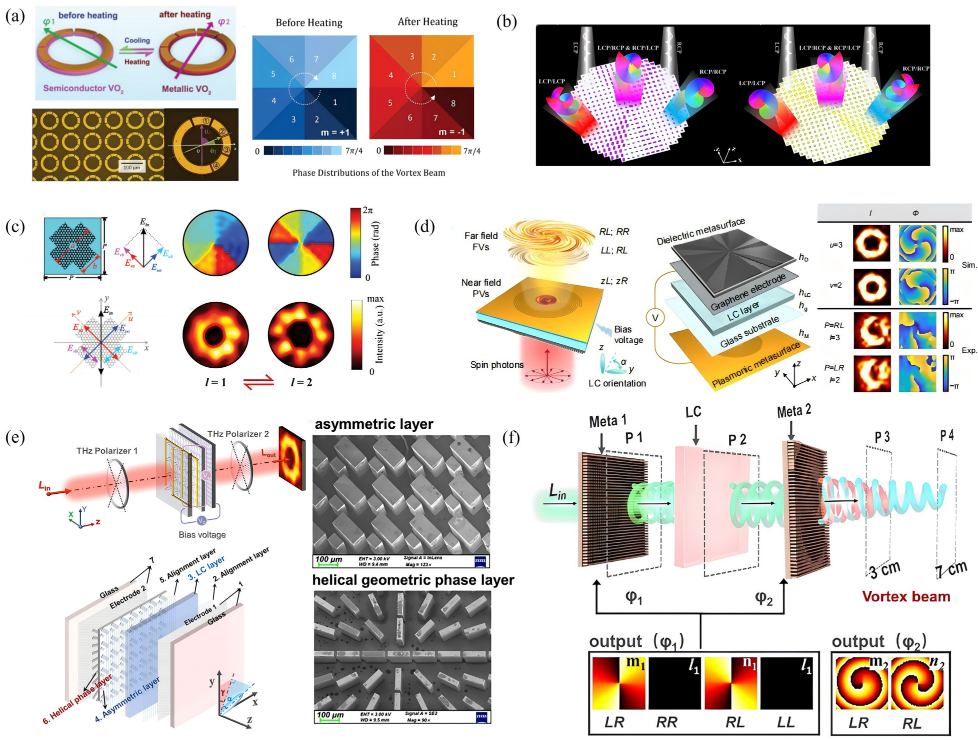

Figure 3.
Control and reconfiguration of structured THz waves with tunable materials and cascaded metasurfaces. (a) VO_2-integrated metasurface enabling thermal switching of $l = \pm 1$ vortices [43]. (b) Thermally reconfigurable multi-channel OAM metasurface [44]. (c) Graphene metasurface [27]. (d) LC-based cascaded device [46]. (e) LC-cascaded metadevice [47]. (f) Schematic of the LC-sandwiched dual-metasurface stack [48].

vortex mode purity [49]. He et al. numerically exploited InSb's thermoplasmonic response in a reflective PB metasurface to realize broadband THz vortex generation ($l = \pm 1, \pm 2, \pm 3$ from ~ 0.65–1.66 THz), with ON/OFF control via global or local heating, suggesting practical routes toward device implementation and scaling to larger apertures [50]. In addition, Nobahar et al. theoretically analyzed magnetically reconfigurable plasma–ferrite stacks with magneto-optic anisotropy, showing joint control of polarization, phase, and THz vortex beam profiles via external magnetic bias, thereby introducing magnetic bias as an additional degree of freedom for OAM wavefront engineering [51]. In practice, VO_2 is attractive for high-contrast switching and "full-space" phase shaping, LCs tend to support near-continuous phase and high vector-beam purity, graphene targets high-speed electrical control, and InSb enables fabrication-friendly thermal tuning. Coordinated use of these materials may approach a balanced compromise among speed, phase depth/ continuity, and loss.

3.2 Reconfigurable and programmable architectures

Beyond material tuning, two complementary paradigms enable real-time wavefront control at the system level: digital coding and photonic phased arrays. First, bit-discrete programmable metasurfaces refresh codewords via low-loss electrical or mechanical actuation. Zhou's group cascaded rotatable transmissive metasurfaces and, via relative rotation, tuned the effective Jones matrix in real time, enabling joint control of the deflection angle (polar/azimuthal steering) and polarization within a single THz device – linking structural reconfiguration to matrix-level programmability (**Figure 4a**) [52]. Second, optically driven photonic phased arrays excite nonlinear PB meta-arrays spatiotemporally using external spatial light modulators, avoiding the insertion loss and bandwidth limitations of RF phase-shifter networks. Using a DMD-programmed nonlinear PB metasurface, they demonstrated 2-bit beam scanning, target (slit) imaging, and OAM generation over 0.8–1.4 THz; the DMD affords kHz-class refresh in principle (the demo was system-limited), with pulse bandwidth and modal flexibility preserved (**Figure 4b**) [41]. Relative to material "gating," these approaches emphasize array–codebook co-design: phase-bit depth, array fill factor, and aperture-normalized sidelobe level jointly determine modal crosstalk and effective isotropic radiated power (EIRP). In practice, 2–3 bits can support robust low-order OAM and multi-beam synthesis; higher bit depths help suppress sidelobes and inter-channel leakage for larger apertures and wider bandwidths [22].

In parallel, passive mechanical and geometric reconfiguration provide ultra-low-loss control on longer time scales. Zhang et al. theoretically proposed and numerically analyzed an all-dielectric metasurface embedding non-Hermitian exceptional points (EPs) to realize exceptional-topological-phase–based decoupling of phase and spin, enabling topologically robust wavefront control under perturbations (**Figure 4c**) [53]. Subsequent theory and experiments showed that, near EPs, spin and phase can be independently tuned, with reduced sensitivity to device deviations and external disturbances [54]. At the programmable-source level, Wang et al. demonstrated programmable exchange-biased spintronic emitters that flexibly generate structured THz waves via laser-assisted magnetization patterning while reducing system loss (**Figure 4d**) [55]. Cheng et al. demonstrated room-temperature, field-free, polarization-controllable ultrafast THz emission from an antiferromagnet/topological-insulator $MnSe/(Bi,Sb)_2Te_3$ heterostructure. Circularly polarized THz pulses (1.0–3.1 THz) arise from the coexistence of magnetic-dipole radiation and spin–charge-conversion–driven electric-dipole radiation; the emitted polarization is tuned by the pump polarization [56]. The results support unified codebook design and coordinated control across the full stack, from on-chip implementations to free-space propagation.

Overall, materials and architectures are complementary across time, space, frequency, and spin–orbit degrees of freedom. Material tuning provides physical time variance and multimodal multiplexing – suited to moderate refresh with substantial phase depth and stable shaping. Programmable architectures deliver system-level real-time control and closed-loop optimization – suited to rapid codebook updates, beam/mode routing, and in-situ calibration. A hierarchical strategy commonly uses high-efficiency geometric/resonant phase as the primary energy path; overlays LCs, graphene, VO_2, and ferroelectric LC media for near-continuous phase with coordinated polarization/amplitude control; and finally employs electronically or optically driven arrays for scene adaptation and residual correction. Employing closed-loop operation with in-situ sensing allows kHz-rate updates that sustain mode purity and link quality, effectively mapping discrete phase control to adaptive, task-oriented reconfiguration [22, 41].

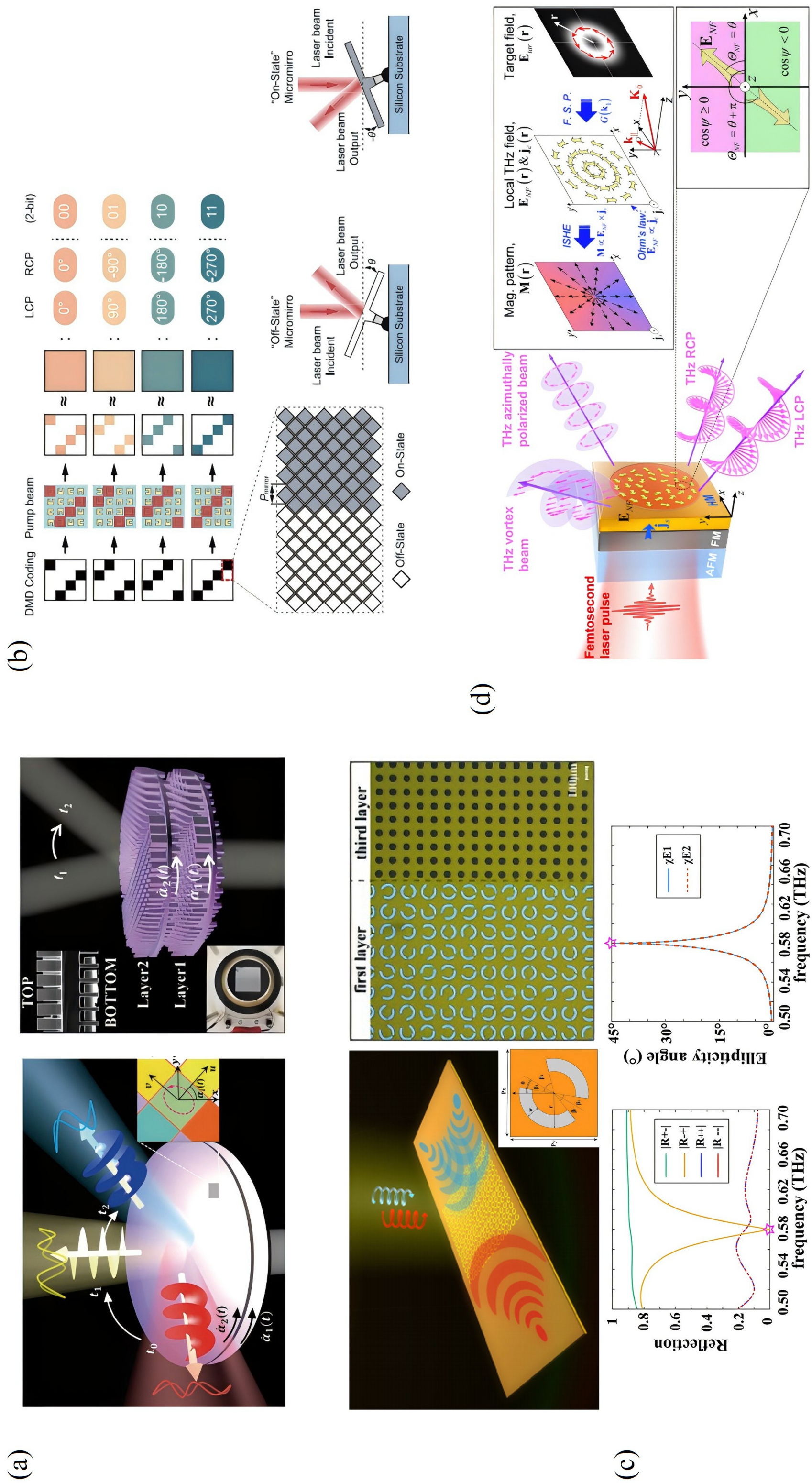

Figure 4.
Reconfigurable and programmable architectures for structured THz control. (a) Cascaded, rotatable metasurfaces [52]. (b) Optically driven photonic THz phased array [41]. (c) Topological metasurface for THz surface-plasmon control [53]. (d) Programmed exchange-biased spintronic THz emitter [55].

4. Multifunctional integration

As generation and control mature, emphasis shifts from feasibility to integrating multiple tasks and channels within a single device or chip. Two directions are particularly relevant: (i) coordinated multiplexing across frequency, polarization, and spatial modes; and (ii) co-design of vector fields with topological properties. The goal is to increase functional density and reconfigurability under constraints of volume and loss.

4.1 Multichannel and polarization multiplexing

Combining geometric and resonant phase, and exploiting polarization and frequency as approximately orthogonal degrees of freedom, has enabled THz devices with increasing multichannel capability. Zhang et al. experimentally demonstrated a chip-integrated, all-silicon polarization-multiplexed metasurface at 1.3 THz that simultaneously generates four-channel orthogonal polarized vortex beams on a single aperture. Under x- and y-polarized incidence, channels 1 and 2 output linear-polarized fundamental vortex states, while channels 3 and 4 produce left- and right-handed circular polarization superposition vortex states. The far-field shows petal-like patterns whose lobe number equals the sum of the topological charges (**Figure 5a**), clearly indicating polarization–OAM multiplexing on a single aperture [57]. Cheng et al. theoretically designed a dual-band reflective metasurface that independently controls linear polarization (0.7 THz, via propagation phase) and circular polarization (1.4 THz, via geometric phase), enabling band-/spin-partitioned beam deflection, planar focusing, and vortex beam generation [58]. Liu et al. numerically demonstrated a transmissive tri-band geometric-phase metasurface that generates OAM modes $l = \pm 1, \pm 2, \pm 3$ at 0.6, 0.857, and 1.892 THz, with mode purity typically exceeding ~ 60%, indicating cross-band modal consistency and multiplexing potential (**Figure 5b**) [59].

On material co-design, Liu et al. theoretically proposed and numerically validated a VO_2-integrated, full-space THz metasurface that thermally switches between transmission and reflection operation (**Figure 5c**) [60]. Li et al. theoretically designed a VO_2-based THz metasurface with anisotropic Z-shaped metal units that switch between transmission and reflection and use PB phase for broadband phase/polarization control [61]. Extending these ideas, Zhang et al. theoretically proposed omnidirectional devices that generate vortices and convert polarization at multiple frequencies in parallel, outlining a multidimensional multiplexing scheme spanning polarization, frequency, OAM, and space (**Figure 5d**) [62].

Overall, these examples reveal a practical breakdown into polarization selection, frequency partition, OAM multiplexing, and spatial routing. In such schemes, polarization separates channels or functions; frequency partitions tasks and links; OAM supplies parallel modal carriers; and spatial control sets beam direction and routing. This factorization can reduce inter-channel crosstalk and simplify separation/filtering along the link, providing a basis for mode-division multiplexing, frequency-division access, and hybrid on-chip/free-space routing. For fabrication and integration, all-dielectric (e.g., silicon) platforms tend to offer high efficiency and bandwidth, whereas phase-change VO_2 provides switchability; their complementarity offers a route to balance efficiency, bandwidth, and reconfigurability within one system.

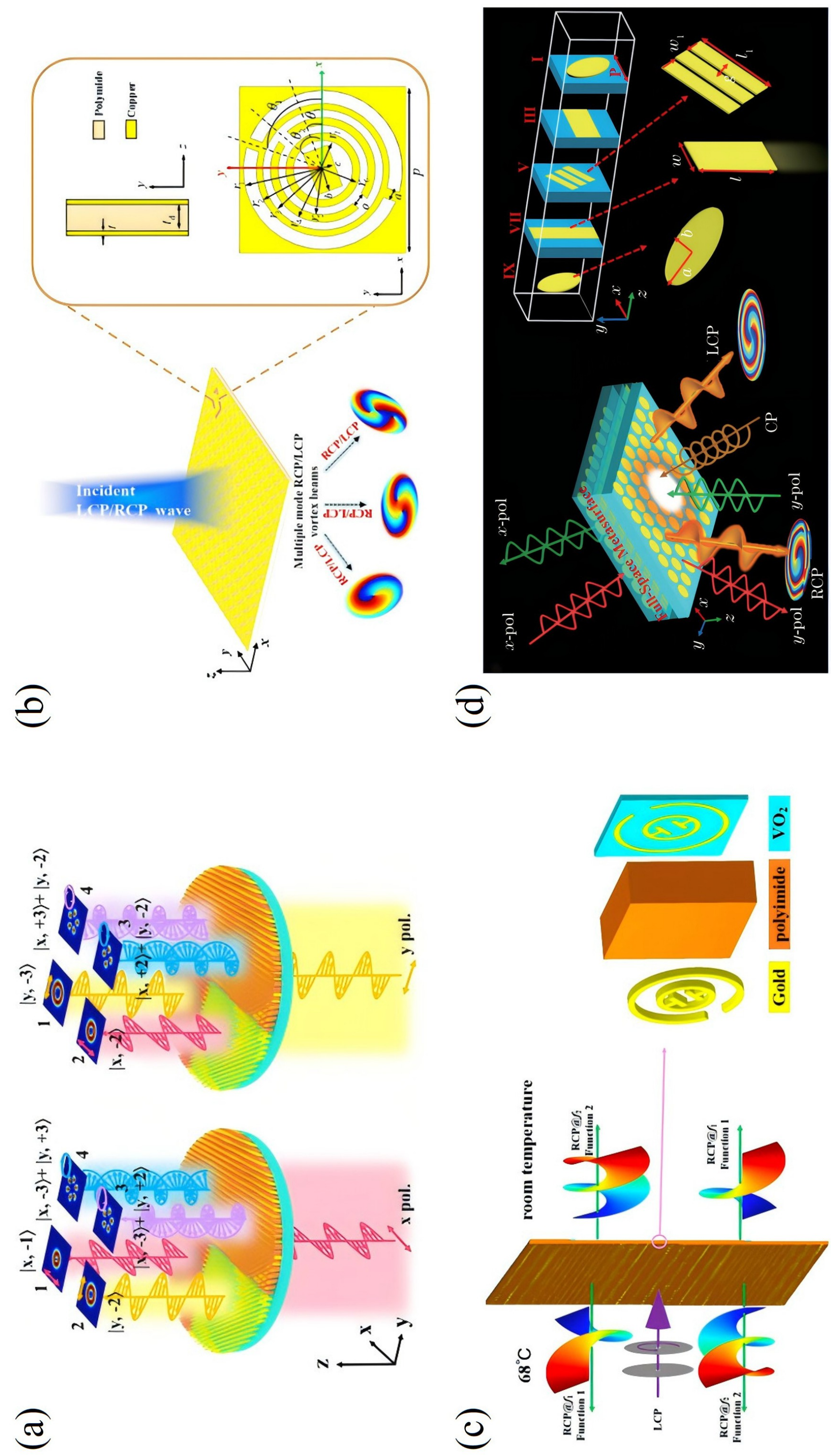

Figure 5.
Multichannel and polarization-multiplexed structured THz generation. (a) Four-channel polarization-multiplexed vortices [57]. (b) Multispectral OAM generator [59]. (c) Dual-frequency bidirectional OAM emitter [60]. (d) Omnidirectional bifunctional THz metasurface [62].

4.2 Hybrid vector–topological design

A second route to multifunctionality is the co-design of vector fields and topological properties, enabling controlled coupling among polarization, OAM, and field profiles during propagation. On low-loss all-dielectric platforms, Yao and co-workers designed anisotropic silicon pillars to independently phase the two circular components and generate THz vector vortex beams with longitudinally varying polarization. The same group demonstrated spin-dependent longitudinal evolution of OAM with an all-dielectric THz metasurface: topological charge transitions from $l = +2$ to -2 under left-circular polarization (LCP) and from $l = +1$ to -1 under right-circular polarization (RCP), along with polarization-state transformations from radial to second-order radial and from azimuthal to radial (**Figure 6a**) [63]. Using an all-silicon metasurface and coherent superposition of orthogonal circularly polarized THz waves via a long focal-depth metalens, the same group realized

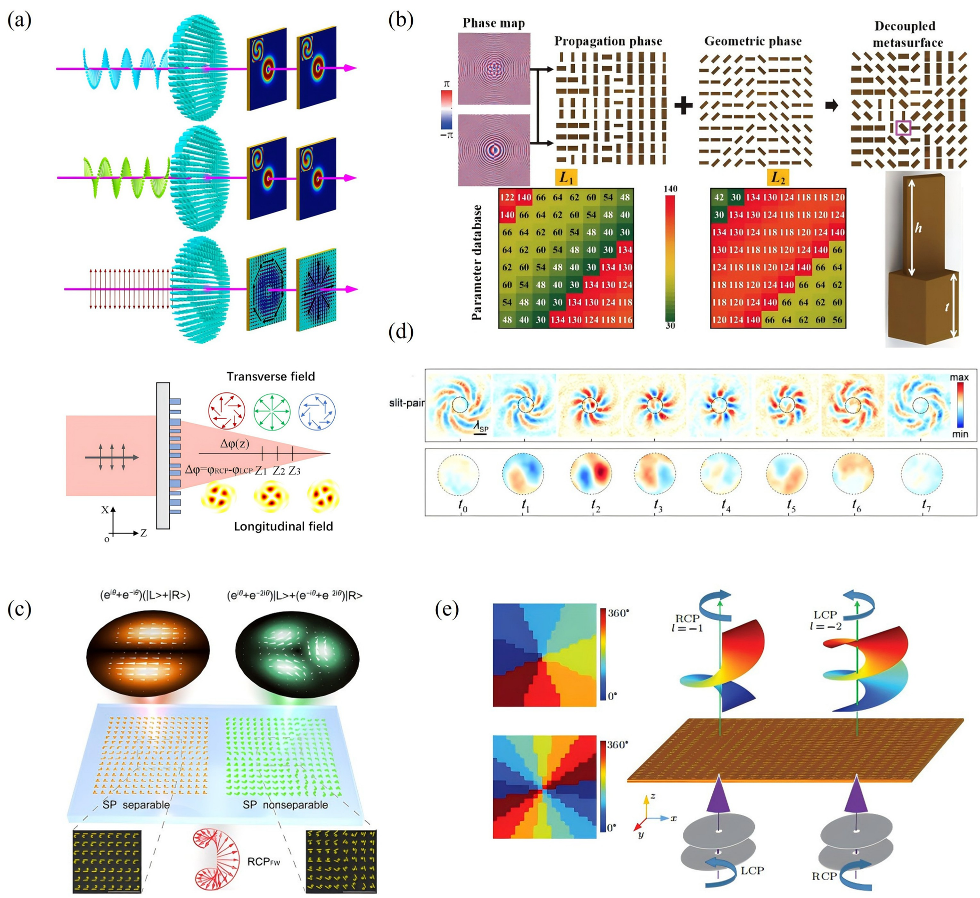

Figure 6.
Hybrid vector–topological control of structured THz fields. (a) All-dielectric metasurfaces generating longitudinally varying vector vortex beams [63]. (b) Single-layer decoupled metasurface integrating propagation and geometric phase [65]. (c) Separation and non-separation schemes enabling near-independent polarization/amplitude control of $l = \pm 1$ *[66]. (d) Time-resolved snapshots of surface-plasmon fields [67]. (e) The phase distribution of vortex beams with* $l = -1$ *and* -2 *under the incidence of LCP and RCP [68].*

structured vector fields along the propagation direction, including continuous variation of the radial (transverse) component and spin–orbit coupling–induced manipulation of the longitudinal component [64]. For channel decoupling, Li et al. used a single-layer silicon metasurface to address LCP/RCP independently near 0.7 THz, encoding off-axis vector vortices with $l = \pm 1$ and ± 6 and enabling rotatable polarization control, indicating joint programmability across spin, orbit, and space (**Figure 6b**) [65]. On a nonlinear platform, Wang et al. developed a chiral nonlinear metasurface offering independent, near-continuous control of polarization and amplitude for vector vortices with $l = \pm 1$, suggesting device-level decoupling between amplitude–polarization parameters and OAM (**Figure 6c**) [66].

Temporal structuring extends control beyond the static phase. With a plasmonic metasurface, Yuan et al. tailored pulse-scale dispersion and phase to reveal transient vortex states and gate their appearance in time, enabling time-resolved handling of topological features (**Figure 6d**) [67]. At the device stack level, Zhong et al. theoretically proposed multilayer switching of focus, OAM order, and polarization on a common platform, suitable for imaging, focusing, and mode routing, with increased complexity balanced against insertion loss (**Figure 6e**) [68]. For cross-band transfer, two NIR phase profiles were programmed and then mapped via type-II DFG to THz, yielding tunable vortices, Bessel beams, and hybrid vortex–Bessel beams with broadband nondiffracting behavior [31]. At the source interface, Pettine et al. employed asymmetric Au nanoantennas on graphene to launch directional nanocurrents under ultrafast drive, coupling electronic degrees of freedom to optical spin and OAM for on-demand radial/azimuthal vector-vortex synthesis; achievable speed and efficiency are set by carrier dynamics and coupling losses [69].

Hybrid design allocates approximately orthogonal resources under finite aperture and loss constraints: geometric/resonant phase with engineered anisotropy for robust generation and interconversion of vector states and OAM; nonlinear and cross-band mapping for complex-field synthesis and nondiffracting transport; and temporal gating/transient dispersion for pulse-scale control of topological features. Multilayer, switchable stacks offer a route to combine static multiplexing with time-varying switching on a common platform. For system translation, open issues include establishing comparable metrology for inter-channel crosstalk and mode purity (harmonized across measurement setups) and tolerance control for broadband, large-aperture fabrication (phase error, sidewall angle, and thickness drift, which can accumulate for higher topological charge l).

5. Applications

5.1 Communications and information processing

For short- to mid-range high-speed interconnects and indoor backhaul, structured THz links are evolving from mode generation toward link-level design. For communications and information processing, such cascaded dielectric–LC–plasmonic modules, with electrically controlled spin–orbit coupling, enable 12-state THz routing and reconfigurable OAM multiplexing under low-voltage drive (**Figure 7a**) [46]. On an all-silicon dielectric metasurface, arranging polarization-maintaining and polarization-conversion meta-atoms enables simultaneous polarization–OAM control with four spatially decoupled linear/circular vortex channels at various charges,

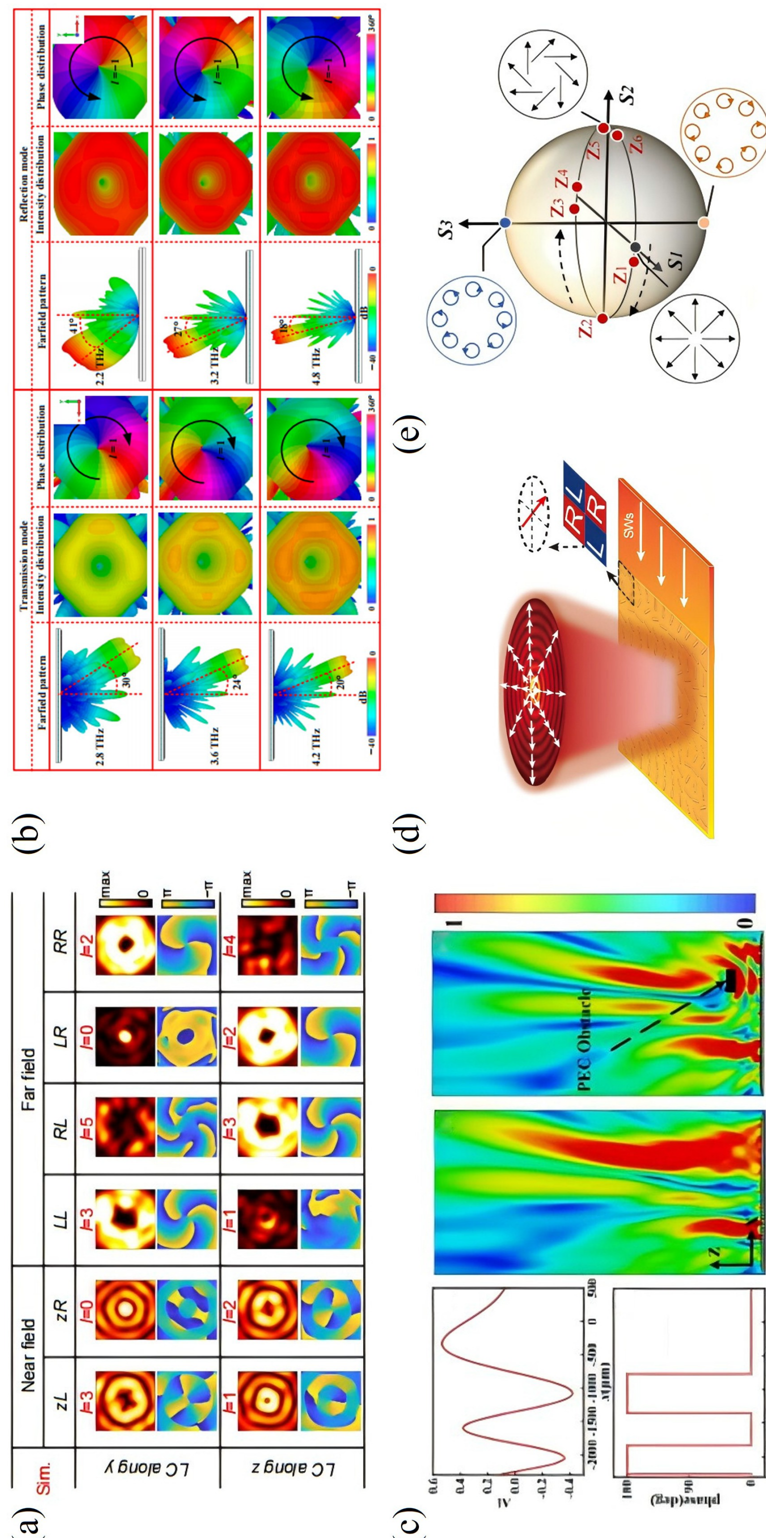

Figure 7.
Communications and sensing using structured THz waves. (a) Cascaded metasurface for 12 OAM modes [46]. (b) Deflected vortex beams [61]. (c) Airy beam generation [16]. (d) SW-to-free-space coupling [36]. (e) Longitudinal evolution of E_x/E_y components in a transmitted vector field [64].

providing added degrees of freedom for parallel multimode THz transmission [57]. Optically driven nonlinear PB phase also enables a programmable THz phased array with 2-bit beam control, real-time imaging, and OAM encoding [41]. Moreover, by switching VO_2 between insulating and metallic states, the same device achieves full-space wavefront shaping – deflected, focused, and nondiffracting vortex beams – in transmission/reflection, enabling dynamically reconfigurable THz links (**Figure 7b**) [61].

Practical design is constrained by EIRP, effective aperture, beam divergence, and power budget [9, 70]; intermodal crosstalk and weather-induced fading can be mitigated by precoding/equalization, multiple input multiple output (MIMO), and data-driven calibration. Receiver design involves trading bit error rate (BER) against coding overhead to balance capacity and reliability [71]. Former studies also indicate that hybrid on-chip/free-space routing is a viable path for short- to mid-range backhaul and indoor high-speed interconnects: on-chip modules handle mode generation/multiplexing and out-coupling, while free-space links provide beam assignment and environmental adaptation. Unified codebooks and in-operation calibration support stable end-to-end links (**Figure 4b**) [41, 46].

5.2 Imaging and sensing

For imaging and sensing, two practical directions have emerged. Nondiffracting and self-accelerating beams (e.g., Bessel and Airy beams) provide an extended depth of field and some tolerance to occlusion and scattering, improving stability in heterogeneous or curved scenes at the cost of power in sidelobes. Wide-aperture vector fields and vector vortices enable selective coupling and multi-parameter interrogation of chirality and anisotropy, provided the generation and detection chains preserve the required polarization and phase structure.

Li et al. demonstrated a reflective Au/polyimide/Au metasurface that generates Airy, dual-Airy, and multi-order/focused vortex beams over 0.8–1.3 THz, exhibiting self-bending and extended depth of field, which can stabilize imaging under scattering; the efficiency is determined by metallic loss and bandwidth (**Figure 7c**) [16]. Nan et al. employed trajectory-phase encoding in a three-layer transmissive metasurface to launch Bessel-like beams on cylindrical helices with rotating polarization, yielding long-DOF, anti-scattering propagation with the expected sidelobe penalty [18]. SW-excited, radially polarized Bessel emission offers high directivity and efficiency, providing a compact, low-loss front end for imaging (**Figure 7d**) [36].

Vector control also supports material-selective probing. Independent LCP/RCP phasing drives longitudinal evolution of E_x/E_y in the transmitted field, enabling z-dependent transverse polarization (with coupled axial control) for anisotropic/chiral excitation; efficiency is limited by dielectric loss and the designed bandwidth (**Figure 7e**) [64]. Zhou et al. used a dual-metal metasurface at 0.14 THz to generate radially polarized vector vortices with selectable topological charge, furnishing polarization–phase templates for anisotropy sensing [72]. These exchange-biased programmable emitters cover the full Poincaré sphere and generate circularly polarized vortices, enabling reconfigurable polarization–OAM states for spatial imaging (**Figure 8c**) [55].

Overall, these studies indicate a system strategy in which, under dose and safety constraints, hollow-beam energy distributions and vector-polarization selectivity

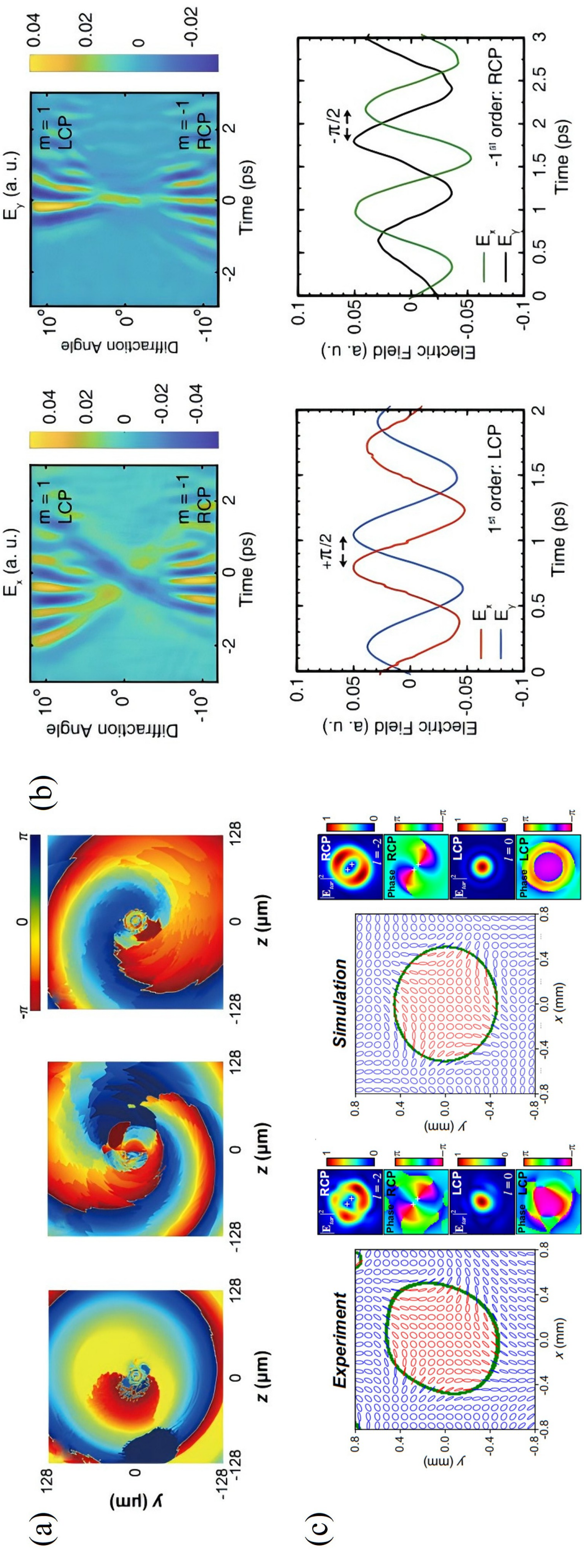

Figure 8.
Strong-field and nonlinear/spintronic THz emitters. (a) Plasma-channel source generating near-GV/m fractional-OAM pulses [42]. (b) Nonlinear PB-metasurface emission [40]. (c) Programmable spintronic THz emitter covering the Poincaré sphere [55].

can enhance tomographic resolution and contrast without increasing total exposure. Coupled with on-chip/free-space bridging and programmable scanning, robust reconstruction can be maintained in complex media and in low-contrast or weak-scattering scenarios, subject to limits set by aperture, efficiency, calibration, and detector bandwidth.

5.3 Strong-field and nonlinear/spintronic emitters

Strong-field platforms are enabling structured THz at application-relevant intensities. In particular, oblique injection into a parabolic plasma channel produces near-GV/m THz vortices with continuously tunable (fractional/near-integer) OAM, offering a high-field, OAM-tunable source for strong-nonlinear spectroscopy and coherent control (**Figure 8a**) [42]. The PB-assisted $\chi^{(2)}$ processes yield broadband, single-cycle THz with spin–orbit decoupling and spatial/mode multiplexing, indicating an on-chip route where emission and wavefront shaping are co-designed (**Figure 8b**) [40]. In an AFM/TI MnSe/$(Bi,Sb)_2Te_3$ heterostructure, optically controllable circularly polarized ultrafast THz emission at room temperature and zero field is achieved via the coexistence of magnetic dipole radiation and spin–charge conversion, with polarization controlled by the excitation laser polarization [56]. The current trend is to move beyond field strength and bandwidth, with increasing emphasis on mode purity, EIRP, and stability. Co-design of emission and shaping in integrated nonlinear devices can reduce downstream loss and improve end-to-end efficiency. Spintronic and plasma sources, however, would benefit from systematic quantification of modal purity and pointing drift, as well as assessments of how these factors impact link performance and imaging stability.

5.4 On-chip coupling, manufacturing, and systemization

Translating structured THz from laboratory demonstrations to deployable platforms is often limited by outcoupling, manufacturability, and interface standardization. Momentum-space BIC provides a compact, alignment-tolerant route to vortex emission, offering robustness and mode purity (**Figure 9a**) [35]. Besides, a SW–excited metasurface forms a low-loss bridge between on-chip and free space: under single SW excitation, it selectively radiates a designated spin channel, and combining two spin channels yields a radially polarized Bessel beam with high directivity (**Figure 9b**) [36].

On fabrication and assembly, projection micro-stereolithography (PμSL), developed by Ke and colleagues, provides scalable, low-cost routes to multi-material, multi-scale meta-optics and lenses. At ~ 0.1 THz, tightly focused shaping of integer and fractional vortices has been demonstrated (**Figure 9c**) [73]. At the system level, optically driven programmable phased arrays have exhibited kHz-rate beam synthesis, scanning, and target recognition, indicating a path toward real-time operation [41]. Combining high-efficiency BIC outcoupling with PμSL/3D-printing scale-up may accelerate progress from controllable field patterns to integrated systems, while motivating harmonized metrology and interface standards for chip-to–free-space interconnects (**Figure 9d**) [74, 75].

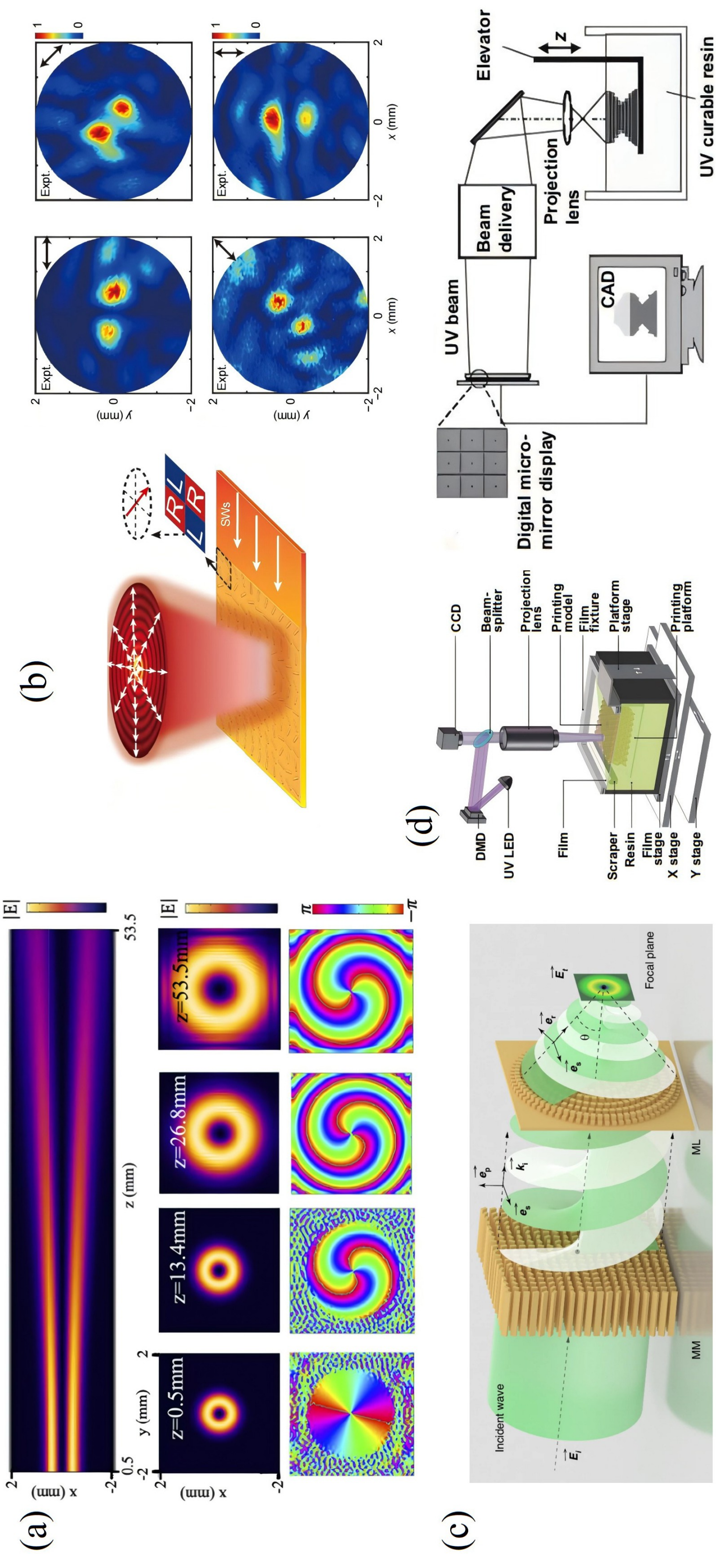

Figure 9.
On-chip coupling, manufacturability, and systemization of structured THz. (a) Momentum-space BIC photonic-crystal emitter [35]. (b) SW-excited metasurface. (c) Schematic diagram of beam conversion by cascade modules [73]. (d) Projection micro-stereolithography (PμSL) [74, 75].

5.5 LC cascading and dynamic evolution

In recent years, significant progress has been made in THz-band photonic devices, particularly in OAM manipulation based on LC-integrated cascaded metasurfaces and research on non-Hermitian systems. In the generation and control of vortex beams, studies have focused on improving mode purity, expanding the degrees of freedom in manipulation, and achieving dynamic reconfiguration. For instance, Wang et al. and Zhao et al. realized multi-modal interference and dynamic encoding of plasmonic vortices and free-space vortices through LC integration and graphene electrodes, respectively, significantly enhancing information capacity and reconfigurability (**Figures 10a** and **b**) [76, 77]. In the same year, Chang's group constructed a multi-channel vortex generator using cascaded metasurfaces and an LC layer, successfully breaking the spin-orbit coupling limitation and achieving high-purity, low-crosstalk multi-mode multiplexing and dynamic switching in both near-field and far-field [46, 48]. In the field of non-Hermitian photonics, Wang et al. and Fu et al. explored the dynamic evolution paths from BICs to higher-order EPs and, for the first time, experimentally observed a third-order EP (EP3) in metasurfaces, providing new mechanisms for highly sensitive sensing and topological photonic control (**Figures 10c** and **d**) [78, 79].

Furthermore, Zhang et al. combined metasurfaces with deep learning to construct a high-dimensional photodetector capable of simultaneously perceiving intensity, polarization, and frequency, expanding the application prospects of photonic devices in intelligent perception and information security [80]. Collectively, these studies have propelled THz photonic devices toward multifunctionality, high dimensionality, programmability, and intelligence, laying a theoretical and experimental foundation for the next generation of integrated photonic chips, high-capacity communication systems, and advanced photoelectric sensing platforms.

6. Conclusion and outlook

THz structured wave now spans passive, active, nonlinear, and programmable layers within system-level architectures (as shown in **Table 1**). NIR pre-encoding mapped to THz by difference-frequency generation or optical rectification provides a practical "pump-in/THz-out" control path, with fidelity limited by phase matching, group-velocity mismatch, and walk-off [31, 41]. SW–to–free-space couplers and all-dielectric multipolar emitters improve extraction efficiency and enable broadband, wide-angle steering within aperture and radiation-loss constraints [36, 37]. Material co-tuning across VO_2, LCs, graphene, and InSb allows trade-offs among channel count, phase coverage/continuity, and speed, with insertion loss and drive power balanced against tuning range [27, 44, 48, 81]. Topological and non-Hermitian controls can add robustness of phase and chirality to fabrication and environmental perturbations [53, 82]. Representative systems report diffraction efficiencies exceeding ~ 80%, cross-polarization conversion near or above 0.9, mode/polarization purity on the order of 70%–80%, modulation depths above ~ 70%, and kHz-rate refresh, supporting OAM-multiplexed links, reconfigurable imaging, and strong-field drivers.

Looking toward application-driven deployment, emphasis shifts from maximizing single metrics to translating multi–degree-of-freedom advantages into measurable,

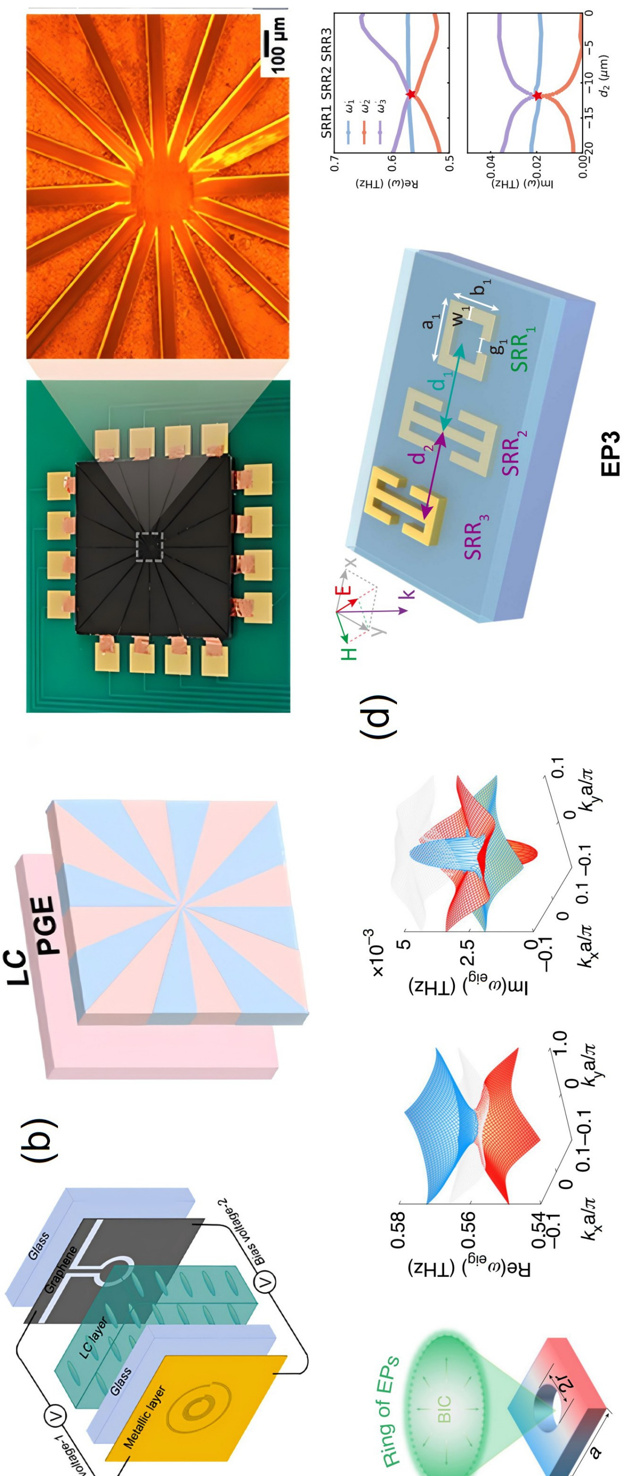

Figure 10.
LC-cascaded THz metasurface and dynamic control of EP. (a) Structure of the THz LC coding PV interferometer [76]. (b) Structure of 16-pixel angular-patterned PGE [77]. (c) Transition from one bound singularity to a two-dimensional exceptional ring. A schematic of the transition of one BIC point to an exceptional ring in a designed unit cell [78]. (d) Schematic diagram of EP3 system [79].

Device name	Material	Control method	Structured wave type (with key performance)	Ref.
Orthogonal I-shaped Reflective PB Metasurface	Metal/ Dielectric	Static (Passive)	Multi-order OAM vortices; simulated reflectance > 90%, 0.8–1.4 THz.	[33]
Multilayer Fabry–Perot Vortex Plate	Metal & Dielectric (3-layer cavity)	Static (Passive)	Broadband THz vortex beams; peak efficiency ~ 65% at 0.5 THz, 0.5–1 THz.	[23]
All-Dielectric Quasi-Perfect Vortex Generator	Silicon pillar array	Static (Passive)	Multi-channel quasi-perfect vortices and spin-distinguished polarization vortices.	[34]
BIC Photonic Crystal Vortex Emitter	Photonic crystal slab (supporting BIC)	Static (Passive)	High-purity, higher-order THz vortex radiation (high-Q modes).	[35]
SW-Excited Vector Bessel Launcher	Metasurface (SW excitation)	Static (Passive)	Radially polarized Bessel beam; high directivity, ~ 90-95% relative efficiency at ~ 0.4 THz.	[36]
Nonlinear PB Vortex Emitting Array	C3 nano-antenna nonlinear array	Optical pumping (Nonlinear)	THz vortex pulses with spin-orbit decoupling: Independent control of frequency, spin, and OAM.	[40]
VO_2-Thermo-Switchable OAM Metasurface	VO_2-integrated metasurface	Thermal (Metal-insulator transition)	Multi-channel OAM beams (l = – 3/–2/–1 and + 1/ + 2/ + 3); switching between states at 1.35–1.39 THz.	[44]
Graphene-Electrotunable Vortex Generator	Graphene metasurface	Electrostatic (Fermi-level tuning)	THz vortex beam with switched topological charge: 2–2.4 THz and 4.5–5.5 THz.	[27, 45]
Liquid-Crystal-Plasmonic Cascaded Metadevice	Dielectric-LC-Plasmonic stack	Electrical (LC reorientation)	12 selectable vortex modes (near- and far-field); low-voltage control, 0.44–0.52 THz.	[46]
LC-Based Vortex-Vector Beam Converter	LC-integrated asymmetric metasurface	Electrical (LC reorientation)	Active conversion between l = ± 2 vortices and cylindrical vector beams; ~ 92% efficiency, ~ 72% modulation depth.	[47]
Nonlinear DFG Tunable Vortex-Bessel Source	Nonlinear crystal (e.g., ZnTe)	Optical encoding (NIR pump, DFG/OR)	Tunable vortices, Bessel beams, and hybrid vortex-Bessel beams; broadband, quasi-nondiffracting.	[31]
Plasma-Channel High-Field OAM Source	Plasma channel	Laser injection (Offset/angle)	High-field (near-GV/m) vortex pulses with tunable fractional/integer OAM (from ~ – 2 to + 2).	[42]

Table 1.
Different approaches for the of thz structured waves.

transferable, and maintainable system gains. Three directions appear promising. First, combine broadband nonlinear emission with low-bit discrete phase tuning using reconfigurable elements. Use nonlinear emitters as low–insertion-loss transmitters/front ends; overlay amplitude or phase tuning via LCs, graphene, or VO_2; and apply in situ, data-assisted calibration to compensate for fabrication tolerances and thermal/ environmental drift. This route aims to improve link capacity, robustness, and power efficiency in practical settings [31, 41, 61]. Second, pursue multiphysics coupling and multidimensional modulation. Add magnetic, strain, and acoustic control channels to the electrical–thermal–optical stack, and co-design transient dispersion and phase in time to make strong-field control, nonlinear spectroscopy, and real-time sensing more reproducible and engineering-ready [40, 42, 82]. Third, develop chip–to–free-space interconnects and a standardized ecosystem. Use SW bridges and BIC-based outcoupling to reduce mode mismatch and divergence, and align efficiency, mode purity, EIRP/BER, and OAM metrology and interoperability. Standardized interfaces would support cross-material/process/platform replication and facilitate networked integration [35, 36, 71].

Furthermore, two directions deserve particular attention for closing the gap between laboratory demonstrations and practical THz systems: patterned ferroelectric nematic LC platforms and spatiotemporal structured beams. Ferroelectric nematic LC films combine low-voltage reorientation with large $\chi^{(2)}$ and a reconfigurable nonlinear PB phase, enabling a single pixelated stack to program phase, amplitude, polarization, and frequency-conversion pathways on-chip; when co-packaged with all-dielectric metasurfaces and SW bridges, they may form compact source–shaping–coupling front ends for adaptive links and mode routing [83–85]. In parallel, spatiotemporal THz beams – wave packets with tailored spatial and temporal characteristics – enable spatiotemporal vortices with transverse OAM, space-time vector beams, and time-varying OAM modes that add orthogonal channels and improve robustness to scattering; together with programmable phased arrays and optical-domain pump mapping, they may support adaptive spatiotemporal control [86–90]. These approaches highlight practical routes toward compact, reconfigurable THz front ends and adaptive spatiotemporal control, which enable measurable gains in capacity, robustness, and power efficiency. In summary, THz structured-beam metasurfaces are a rapidly developing field, with progress from device concepts to system-level demonstrations, and we believe continued co-design of sources, metasurfaces, and interconnects will enable scalable, application-ready systems.

Author details

Wei Chen, Zhong-Ze Peng†, Ling-Ling Ma* and Yan-Qing Lu

Key Laboratory of Intelligent Optical Sensing and Manipulation, College of Engineering and Applied Sciences, Collaborative Innovation Center of Advanced Microstructures, National Laboratory of Solid State Microstructures, Nanjing University, Nanjing, China

† The authors contribute equally.

*Address all correspondence to: malingling@nju.edu.cn

References

[1] Siegel PH. Terahertz technology. IEEE Transactions on Microwave Theory and Techniques. 2002;**50** (3):910–928

[2] Lee Y-S. Principles of Terahertz Science and Technology, Vol. **170**. New York, NY: Springer Science & Business Media; 2009

[3] Song H-J, Nagatsuma T. Present and future of terahertz communications. IEEE Transactions on Terahertz Science and Technology. 2011;**1**(1):256–263

[4] Hamza MN, et al. High-performance THz nanometamaterial absorber with negative permittivity (0.1–10 THz) for early cancer detection via circulating exosomes. IEEE Sensors Journal. 2025;**25**:34716–34733

[5] Hamza MN, et al. A 50THz ultra-wideband nano-photonics perfect absorber biosensor for label-free detection of circulating cancer exosomes: Advancing early cancer diagnostics. IEEE Photonics Journal. 2025;**17**:1–16

[6] Hamza MN, et al. Precision multiband terahertz metamaterial biosensor with targeted spectral selectivity for early detection of MCF-7 breast cancer cells. IEEE Sensors Journal. 2025;**25**:14970–14987

[7] Hamza MN, et al. Terahertz dual-band metamaterial biosensor for cervical-cancer diagnostics. IEEE Photonics Journal. 2024;**16**:1–11

[8] Hamza MN, et al. Designing a high-sensitivity microscale triple-band biosensor based on terahertz MTMs to provide a perfect absorber for non-melanoma skin cancer diagnostic. IEEE Photonics Journal. 2024;**16**:1–13

[9] Alibakhshikenari M, et al. A comprehensive survey on antennas on-chip based on metamaterial, metasurface, and substrate integrated waveguide principles for millimeter-waves and terahertz integrated circuits and systems. IEEE Access. 2022;**10**:3668–3692

[10] Alibakhshikenari M, et al. Compact and Low-Profile On-Chip Antenna Using Underside Electromagnetic Coupling Mechanism for Terahertz Front-End Transceivers. Electronics 2021;**10**:1264

[11] Salén P, et al. Matter manipulation with extreme terahertz light: Progress in the enabling THz technology. Physics Reports. 2019;**836-837**:1–74

[12] Allen L, et al. Orbital angular momentum of light and the transformation of Laguerre-Gaussian laser modes. Physical Review A 1992;**45**:8185

[13] Yao AM, Padgett MJ. Orbital angular momentum: Origins, behavior and applications. Advances in Optics and Photonics. 2011;**3**(2):161–204

[14] Durnin J, Miceli Jr J, Eberly JH. Diffraction-free beams. Physical Review Letters. 1987;**58**(15):1499

[15] Siviloglou GA, et al. Observation of accelerating airy beams. Physical Review Letters. 2007;**99**(21):213901

[16] Li J-S, Zhong M. Airy beam multifunctional terahertz metasurface.

IEEE Photonics Technology Letters. 2023;**35**(5):245–248

[17] Zhan Q. Cylindrical vector beams: From mathematical concepts to applications. Advances in Optics and Photonics. 2009;**1**(1):1–57

[18] Nan T, et al. Generation of structured light beams with polarization variation along arbitrary spatial trajectories using tri-layer metasurfaces. Opto-Electronic Science 2024;**3**:230052–230052

[19] Al-Naib I, Withayachumnankul W. Recent progress in terahertz metasurfaces. Journal of Infrared, Millimeter, and Terahertz Waves. 2017;**38**(9):1067–1084

[20] Zang X, et al. Metasurfaces for manipulating terahertz waves. Light: Advanced Manufacturing 2021;**2**: 148–172

[21] Minasyan A, et al. Geometric phase shaping of terahertz vortex beams. Optics Letters 2016;**42**:41

[22] Cui TJ, et al. Information metamaterial systems. iScience 2020;**23**:101403

[23] Niu L, et al. Metasurface-empowered high-efficiency and broadband terahertz vortex beam plates. Applied Physics Letters. 2024;**124**(8):081701

[24] Fan J, Cheng Y. Broadband high-efficiency cross-polarization conversion and multi-functional wavefront manipulation based on chiral structure metasurface for terahertz wave. Journal of Physics D: Applied Physics. 2020;**53**(2):025109

[25] Jiaoyan G, et al. Generation of broadband terahertz vortex beam based on double-arrow metasurface. Chinese Journal of Lasers. 2021;**48**(20):2014003

[26] Huang F, et al. Generating terahertz perfect vortex beam via all-dielectric metasurface. In: 2023 48th International Conference on Infrared, Millimeter, and Terahertz Waves (IRMMW-THz). IEEE; 2023

[27] Chen D, et al. Tunable polarization-preserving vortex beam generator based on diagonal cross-shaped graphene structures at terahertz frequency. Advanced Optical Materials. 2023;**11** (14):2300182

[28] Shen Z, et al. Liquid-crystal-integrated metadevice: Towards active multifunctional terahertz wave manipulations. Optics Letters. 2018;**43**:4695–4698

[29] Shen Z, et al. Liquid crystal integrated metalens with tunable chromatic aberration. Advanced Photonics. 2020;**2**:036002–036002

[30] Wang L, et al. Graphene-assisted high-efficiency liquid crystal tunable terahertz metamaterial absorber. Optics Express. 2017;**25**:23873–23879

[31] Lin Q, et al. A universal and versatile terahertz field manipulation mechanism by manipulating near-infrared phases with a dislocation scheme. Nature Communications. 2025;**16**:6656

[32] Ren Z, et al. Terahertz metamaterials inspired by quantum phenomena. Research. 2025;**8**:0597

[33] Li X, Zhou L, Zhao G. Terahertz vortex beam generation based on

reflective metasurface. Acta Physica Sinica. 2019;**68**(23):238101

[34] Huang F, et al., Generating terahertz perfect vortex beam via all-dielectric metasurface. In: 2023 48th International Conference on Infrared, Millimeter, and Terahertz Waves (IRMMW-THz). 2023. p. 1–2

[35] Bai T, et al. Terahertz vortex beam generator based on bound states in the continuum. Optics Express. 2021;**29**:25270–25279

[36] Wang Z, et al. Efficient generation of vectorial terahertz beams using surface-wave excited metasurfaces. Opto-Electronic Science. 2025;**4**:240024–240024

[37] Peng S, et al. All-dielectric asymmetric metagrating for broadband and wide-angle terahertz beam steering with high efficiency. Advanced Functional Materials. 2025;**36**(3):e12746

[38] Dhaybi AA, et al. Terahertz vortex beam generation by infrared vector beam rectification. Journal of the Optical Society of America B. 2018;**36**:12–18

[39] Mou S, et al. Generation of terahertz vector beam bearing tailored topological charge. APL Photonics. 2023;**8**(3):036103

[40] McDonnell C, et al. Functional THz emitters based on pancharatnam-berry phase nonlinear metasurfaces. Nature Communications. 2021;**12**:30

[41] Niu L, et al. Photonic terahertz phased array via selective excitation of nonlinear Pancharatnam-Berry elements. Nature Communications. 2025;**16**:8159

[42] Wang L, et al. Terahertz vortices with tunable topological charges from a laser–plasma channel. Advanced Photonics Nexus. 2025;**4**(03):036004

[43] Dong B, et al. Switchable pancharatnam–berry phases in heterogeneously integrated THz metasurfaces. Advanced Materials. 2024;**37**(6):2417183

[44] Guo K, Xin J, Song Z. Terahertz six-channel metasurface for the dynamic modulation of OAM. Journal of Physics D: Applied Physics. 2024;**58**(6):065109

[45] Ma H, et al. A broadband vortex beam generator using graphene metasurface reflectarray in terahertz region. Physica Scripta. 2022;**97**(12):125506

[46] Wang Y, et al. Terahertz active multi-channel vortices with parity symmetry breaking and near/far field multiplexing based on a dielectric-liquid crystal-plasmonic metadevice. Opto-Electronic Advances. 2025;**8**:240250

[47] Zhao H, et al. Vortex-vector beam conversion and chiral field manipulation based on terahertz liquid crystal cascaded metadevice. Laser & Photonics Reviews. 2024;**18**(10):2400442

[48] Zhao H, et al. Active broadband terahertz OAM-based metalens based on multi-channel multiplexing. Laser & Photonics Reviews. 2025;**19**(12):2402084

[49] Yang Q, et al. Broadband transparent terahertz vortex beam generator based on thermally tunable geometric metasurface. Optical Materials. 2021;**121**:111574

[50] He B, et al. Broadband and thermally switchable reflective metasurface based on Z-shape InSb for terahertz vortex beam generation. Physica E: Low-dimensional Systems and Nanostructures. 2022;**144**:115373

[51] Nobahar D, Khorram S. Terahertz vortex beam propagation through a magnetized plasma-ferrite structure. Optics & Laser Technology. 2022;**146**:107522

[52] Cai X, et al. Dynamically controlling terahertz wavefronts with cascaded metasurfaces. Advanced Photonics. 2021;**3**(03):036003

[53] Zhang Y, et al. Vortex beam generator based on exceptional topological phase in terahertz all-dielectric metasurface. Applied Physics Express. 2023;**16**(9):092002

[54] Lang Y, et al. Topological metasurface for spin-decoupled wavefront manipulation of terahertz surface plasmons. Laser & Photonics Reviews. 2024;**19**(4):2401281

[55] Wang S, et al. Flexible generation of structured terahertz fields via programmable exchange-biased spintronic emitters. eLight. 2024;**4**:1–13

[56] Cheng Y, et al. Antiferromagnet-topological insulator heterostructure for polarization-controllable terahertz generation. Nature Communications. 2025;**16**:5656

[57] Zhang Q, et al. Chip-integrated polarization multiplexed metasurface for simultaneous generation of versatile terahertz vortices. Nanophotonics. 2025;**14**:2219–2228

[58] Cheng Y, et al. Dual-band terahertz reflective-mode metasurface for the wavefront manipulation of independent linear and circular polarization waves. Journal of the Optical Society of America B. 2024;**41**:341

[59] Liu J, et al. Tri-band terahertz vortex beam generator based on a completely independent geometric phase metasurface. Journal of the Optical Society of America B. 2023;**40**:441

[60] Li J, et al. Bidirectional terahertz vortex beam regulator. Materials. 2022;**15**:8639

[61] Li X, et al. Full-space wavefront shaping of broadband vortex beam with switchable terahertz metasurface based on vanadium dioxide. Nanomaterials. 2023;**13**:3023

[62] Lina Z, Jiusheng L. Omnidirectional dual-function terahertz metasurface device. Acta Optica Sinica. 2024;**44**(3):0323001

[63] Zheng C, et al. Creating longitudinally varying vector vortex beams with an all-dielectric metasurface. Laser & Photonics Reviews. 2022;**16**(10):2200236

[64] Li J, et al. Structured vector field manipulation of terahertz wave along the propagation direction based on dielectric metasurfaces. Laser & Photonics Reviews. 2022;**16**(12):2200325

[65] Li H, et al. Binary encoding-inspired generation of vector vortex beams. Science china physics. Science China Physics, Mechanics & Astronomy. 2023;**66**(5):254212

[66] Wang Q, et al. Nonlinear metasurfaces for completed control of amplitude, phase, and polarization in

broadband terahertz generation. Advanced Materials. 2025;**37**(30):2500392

[67] Yuan X, et al. Temporally deuterogenic plasmonic vortices. Nanophotonics. 2024;**13**:955–963

[68] Zhong M, Li J-S. Switchable vortex beam polarization state terahertz multi-layer metasurface. Chinese Physics B. 2022;**31**(11):309–315

[69] Pettine J, et al. Light-driven nanoscale vectorial currents. Nature. 2024;**626**:984–989

[70] Alibakhshikenari M, et al. Study on improvement of the performance parameters of a novel 0.41-0.47 THz on-chip antenna based on metasurface concept realized on 50 mum GaAs-layer. Scientific Reports. 2020;**10**(1):11034

[71] Xu C, et al. Reconfigurable terahertz metamaterials: From fundamental principles to advanced 6G applications. Iscience. 2022;**25**(2):103799

[72] Zhou H, et al. Ultrathin freestanding terahertz vector beam generators with free phase modulation. Optics Express. 2021;**29**:1384

[73] Ke L, et al. Tight focusing of fractional-order topological charge vector beams by cascading metamaterials and metalens. Microsystems & Nanoengineering. 2024;**10**:1–17

[74] Ge Q, et al. Projection micro stereolithography based 3D printing and its applications. International Journal of Extreme Manufacturing. 2020;**2**(2):022004

[75] Peng ZZ, et al. Magnetic field enhanced frequency-selective terahertz detection via 3D printing micro-helical stepped and MoTe2 coated arrays. Advanced Optical Materials. 2025;**13**(1):2401956

[76] Wang Y, et al. Spatiotemporal coding terahertz plasmonic vortex on-chip interferometer. Laser & Photonics Reviews. 2025;e01608

[77] Zhao H, et al. Programmable terahertz grafted vortex interference based on patterned transparent electrodes and liquid crystal anisotropy-induced chiral field. Advanced Functional Materials. 2025;e19749

[78] Wang L, et al. Photoswitchable exceptional points derived from bound states in the continuum. Light: Science & Applications. 2025;**14**:377

[79] Fu P, et al. Achieving higher-order exceptional points in a terahertz metasurface. Nano Letters 2025;**25**:3773–3780

[80] Zhang ZK, et al. Deep learning-enabled ultra-broadband terahertz high-dimensional photodetector. Nature Communications. 2025;**16**:8133

[81] Nie R, et al. Vanadium dioxide-based terahertz metasurfaces for manipulating wavefronts with switchable polarization. Optics & Laser Technology. 2023;**159**:109010

[82] Ren Z, et al. Terahertz metamaterials inspired by quantum phenomena. Research. 2025;**8**:1–28

[83] Pan J-T, et al. Nonlinear geometric phase coded ferroelectric nematic fluids for nonlinear soft-matter photonics. Nature Communications. 2024;**15**:8732

[84] Chen H-F, et al. Reconfigurable nonlinear pancharatnam-berry diffractive optics with photopatterned ferroelectric nematics. Light: Science & Applications. 2025;**14**:314

[85] Li C-Y, et al. Domain engineering in ferroelectric nematics for nonlinear optical modulation. Science Advances. 2025;**11**(28):eadu7362

[86] Chong A, et al. Generation of spatiotemporal optical vortices with controllable transverse orbital angular momentum. Nature Photonics. 2020;**14**:350–354

[87] Chen W, et al. Time diffraction-free transverse orbital angular momentum beams. Nature Communications. 2022;**13**:4021

[88] Chen W, et al. Observation of chiral symmetry breaking in toroidal vortices of light. Physical Review Letters. 2024;**132**(15):153801

[89] Liu X, Cao Q, Zhan Q. Spatiotemporal optical wavepackets: From concepts to applications. Photonics Insights. 2024;**3**(4):R08

[90] Chen W, et al. Tailoring spatiotemporal wavepackets via two-dimensional space-time duality. Nature Communications. 2025;**16**:2818